

Noncentrosymmetric superconductor BaRhSi₂

Masaaki Isobe,^{1,*} Koji Kimoto,² and Masao Arai,³ Taras Kolodaizhnyi⁴, and Eiji Takayama-Muromachi¹

¹ National Institute for Materials Science (NIMS), 1-2-1 Sengen, Tsukuba, Ibaraki 305-0047, Japan

² Center for Basic Research on Materials, National Institute for Materials Science (NIMS),
1-2-1 Sengen, Tsukuba, Ibaraki 305-0047, Japan

³ Center for Basic Research on Materials, National Institute for Materials Science (NIMS),
1-1 Namiki, Tsukuba, Ibaraki 305-0044, Japan

⁴ National Institute for Materials Science (NIMS), 1-1 Namiki, Tsukuba, Ibaraki 305-0044, Japan

(Revised: March 2026)

Barium-rhodium silicide BaRhSi₂ has been successfully synthesized using a high-pressure technique at 6GPa. X-ray Rietveld analysis and scanning transmission electron microscopy studies revealed that BaRhSi₂ is isostructural to BaIrSi₂, within the noncentrosymmetric space group C222₁ with the lattice parameters: $a = 14.9777(1)$ Å, $b = 8.0517(1)$ Å and $c = 8.0551(1)$ Å. Electrical resistivity, magnetic moment, and specific heat measurements indicate that BaRhSi₂ is a type-II superconductor with a critical temperature $T_c \sim 5.1$ K, an upper critical field $H_{c2}(0) \sim 32$ kOe and a Ginzburg-Landau parameter $\kappa_{GL} \sim 56$. The superconductivity is a Bardeen-Cooper-Schrieffer (BCS)-like state with moderate electron-phonon coupling $\lambda_{ep} \sim 0.6$ and weak electron correlation $\lambda_{ee} \sim 0.1$. Phonon mediation seems to be dominant for the Cooper pairing. The *ab initio* calculations revealed that BaRhSi₂ has three pairs of Fermi surfaces split by spin-orbit coupling. The band splitting energy is around $\Delta_{ASO} \sim 0.03$ eV near E_F , which is rather smaller than that (~ 0.07 eV) in BaIrSi₂.

* Contact author: ISOBE.Masaaki@nims.go.jp

ORCID

Masaaki Isobe	https://orcid.org/0000-0002-3201-8489
Kohji Kimoto	https://orcid.org/0000-0002-3927-0492
Masao Arai	https://orcid.org/0000-0003-0088-5649
Taras Kolodiazhnyi	https://orcid.org/0000-0002-9630-9461
Eiji Takayama-Muromachi	https://orcid.org/0000-0001-7819-4317

I. INTRODUCTION

There has been much interest in the electronic state and possible superconductivity associated with large spin-orbit coupling (SOC) in heavy element compounds such as the iridates [1]. In this sense, one of the recent topics of interest is “noncentrosymmetric superconductivity”, in which the crystal structure lacks spatial inversion symmetry. It has been theoretically predicted that the absence of inversion symmetry can lead to unconventional superconductivity [2-8]. In noncentrosymmetric systems, the asymmetric atomic positioning induces a local electric field gradient in the unit cells, which lifts the twofold spin degeneracy of the electronic band through the SOC and splits the Fermi surface into two spin-nondegenerate surfaces. When such an electron system is transferred into a superconducting state at low temperature, the Cooper pairs can be formed as a parity-mixed state, in which its wave function is composed of both the spin-singlet and -triplet characteristics with an admixture of even and odd parity. The parity-mixed state is expected to give rise to a two-component superconducting gap order parameter. The actual superconducting gap structure depends on the relative amplitudes and angular distributions of the singlet and triplet components. In some cases, line nodes can appear on a Fermi surface, yielding an anisotropic superconductivity [9, 10]. The nodal anisotropic gap structure can be detected by experiments such as nuclear-spin relaxation [11] and specific-heat measurements. In addition, the unusual electronic state can generate an extremely large upper critical field H_{c2} beyond the Pauli limit. These phenomena are considered to be originally attributed to large antisymmetric spin-orbit coupling (ASOC) for noncentrosymmetric electron systems.

The parity mixing state might be controllable by tuning the ASOC, which may possibly change the mixing ratio of the spin-singlet and -triplet pairing channel in some cases. This hypothesis is based on the report that for the $\text{Li}_2(\text{Pd}_{1-x}\text{Pt}_x)_3\text{B}$ system, stronger ASOC increases the spin-triplet component [12, 13]. In addition, electronic correlation also affects the superconducting state, since it often facilitates an interaction between the different pairing channels. In fact, the unusual large H_{c2} can be observed in the strongly correlated heavy-fermion systems, CePt_3Si [14], CeRhSi_3 [15], and CeIrSi_3 [16]. In these systems, the large effective mass of electrons can lead to a greatly enhanced orbital limit of H_{c2} , making it easier to see if Pauli limit of H_{c2} is missing due to ASOC. Another curious aspect is time-reversal symmetry breaking (TRSB) in superconductivity, as it suggests the presence of complex order parameters in the anisotropic superconducting state. TRSB can be detected by muon spin rotation (μSR) experiments. To date, only a few noncentrosymmetric superconductors have been found to exhibit TRSB, such as LaNiC_2 [17], Re_6Zr [18], Zr_3Ir [19], *etc.* Our primary interest lies in the relationship between ASOC and parity-mixed states, as well as TRSB in asymmetric superconductivity. So far, many superconductors without centrosymmetry in their crystal structures have been known; however, there are not so many that exhibit anomalous features characteristic of the

anisotropic superconducting state essentially caused by the spatial inversion symmetry breaking. The fact that there are a few materials exhibiting the intrinsic properties of noncentrosymmetric superconductivity makes it difficult to clarify the essential role of ASOC and electron correlation in noncentrosymmetric superconductivity. It is therefore required to search for more superconductors with spatial inversion symmetry breaking, which is expected to trigger further progress in understanding of noncentrosymmetric superconductivity.

In 2019, the present authors reported the BaIrSi₂ ($T_c \sim 6$ K) superconductor with a unique noncentrosymmetric crystal structure [20]. It was found that the crystal structure contains significantly distorted Ir-Si polyhedrons, which are responsible for the ASOC arising from an asymmetric crystal field around the Ir atom. In fact, *ab initio* density function theory (DFT) calculations showed that BaIrSi₂ has Fermi surfaces that split into two due to ASOC. It is interesting to look for family compounds with the same structure as BaIrSi₂, to see the effect of ASOC on the superconducting ground state. As a result of many trials of various materials, we have recently succeeded in synthesizing a related compound, BaRhSi₂. In this paper, we report details of the crystal structure, the superconducting properties, and the DFT electronic structure of the noncentrosymmetric superconductor BaRhSi₂. We compare BaRhSi₂ with BaIrSi₂, in terms of the superconducting parameters and the size of Fermi surface splitting due to ASOC.

II. EXPERIMENTAL DETAILS

Polycrystalline samples of BaRhSi₂ were prepared from a stoichiometric mixture of the reagents, BaSi₂ (2N) and Rh (3N) powders, by solid-state reaction using the high-pressure synthesis technique. The mixture was pressed into a pellet 6.9 mm in diameter and ~4mm in thickness (weight: ~400 mg). The process steps of weighing, mixing and pellet formation were carried out in a glove box filled with dry argon gas to prevent oxidation. The pellets were placed in a high-pressure cell with a pressure medium of hexagonal boron nitride (h-BN) powder, and then reacted at 1,600 °C for 1 hour under 6 GPa using a flat-belt-type high-pressure apparatus, followed by quenching to room temperature before pressure release.

Phase purity and crystal structure of the products were studied using conventional powder x-ray diffraction (XRD). The XRD data were collected at room temperature using a diffractometer (Rigaku, SmartLab3) equipped with a Cu K_α radiation source. To confirm that the major phase in the ceramic sample is BaRhSi₂, electron probe microanalysis (EPMA) was performed using a field-emission type analyzer (JEOL, JXA-8500F) operated at 15 kV; BaAl₄, Rh, and Si were used as the standard materials. The crystal structure of BaRhSi₂ was observed using a high-resolution scanning transmission electron microscope (STEM; FEI, Titan Cubed) operating at 300 kV, equipped with a spherical aberration (Cs-)

corrector (CEOS GmbH, DCOR). Customized software was used to improve the S/N ratio of the STEM images [21]. The structural parameters were refined by the x-ray Rietveld method using the RIETAN-FP analysis software [22]. Electrical resistivity was measured by the standard dc four-probe method with an excitation current of ~ 5 mA using a commercial instrument (Quantum Design, physical properties measurement system (PPMS)). The typical sample geometry parameters were ~ 2.2 mm² for a cross-section and ~ 0.6 mm in length between the voltage electrodes. Specific heat was measured on cooling for a small bulk specimen (weight: ca. 7.8 mg) using the time-relaxation method with the PPMS. Static magnetic data were collected for a pulverized sample (weight: ca. 92 mg) using a SQUID magnetometer (Quantum Design, magnetic properties measurement system (MPMS)).

The *ab initio* electronic structure calculations were performed by means of the full-potential linearized augmented plane-wave (FLAPW) method using the WIEN2k software package [23, 24]. The generalized gradient approximation (GGA) [25], based on the DFT [26], was employed as the exchange-correlation energy functional. The spin-orbit interaction is included as a perturbation to the scalar-relativistic equations. Experimental lattice parameters and atomic coordinates were used for the calculation. The muffin-tin sphere radii (R) were chosen as 2.5 a.u. for Ba, 2.4 a.u. for Rh, and 1.83 a.u. for Si. The self-consistent calculations were converged well with the wave-number cutoff parameter K , satisfying $R_{\min} \times K = 7$, where R_{\min} is the smallest muffin radius of 1.83 a.u. The Brillouin zone (BZ) integration for self-consistent calculations was approximated by a tetrahedron method with the BZ divided into $8 \times 8 \times 7$ uniform mesh, resulting in 80 k -points in the irreducible Brillouin zone (IBZ). For the density of states (DOS) and the Fermi-surface plot, eigen-energies were computed using up to $28 \times 28 \times 24$ mesh, consisting of 2,743 k -points in the IBZ.

III. RESULTS AND DISCUSSION

A. Crystal structure

Figure 1 (a) shows a powder XRD profile of the sample. The sample is nearly monophasic; most of the Bragg peaks in the XRD profile are assignable to BaRhSi₂ [27]. The reflections can be systematically indexed with a C -centered orthorhombic Bravais lattice of $a = 14.9777(1)$ Å, $b = 8.0517(1)$ Å, and $c = 8.0551(1)$ Å. Extinctions of the reflections are $h + k = 2n$ for hkl , $k = 2n$ for $0kl$, $h = 2n$ for $h0l$, $h + k = 2n$ for $hk0$, $h = 2n$ for $h00$, $k = 2n$ for $0k0$, and $l = 2n$ for $00l$. Possible space groups are, therefore, only noncentrosymmetric $C222_1$ (No. 20). The space group, the lattice parameters, and the intensity pattern are similar to those of BaIrSi₂ ($C222_1$, $a = 15.0492(1)$ Å, $b = 8.0311(1)$ Å, and $c = 8.0314(1)$ Å [20]), obviously suggesting that the present compound BaRhSi₂ is isostructural to BaIrSi₂. The atomic composition of the phase was measured using the EPMA method for selected ten crystal grains in the ceramic sample. The average molar ratio of Ba : Rh : Si (= 24.2(3)) :

24.1(2) : 51.7(5) at. %) is nearly 1 : 1 : 2. This ensures that the observed phase is BaRhSi₂.

The crystal structure of BaRhSi₂ was more precisely studied using the Rietveld analysis of the XRD data. The initial structure model was assembled with reference to the structure of BaIrSi₂. Figure 1 (a) is the x-ray profile of the Rietveld refinement, where resultant reliability factors are $R_{WP} = 6.89\%$, $R_B = 1.29\%$, $R_F = 0.50\%$, and $S = R_{WP}/R_e = 0.949$. The observed XRD pattern is reproduced by the analysis with the proposed structure model. The refined structure parameters of BaRhSi₂ are summarized in Table 1. Figure 1 (b) is an illustration of the crystal structure of BaRhSi₂, depicted using the refined coordinates. The structure contains two kinds of Si polyhedrons surrounding Rh atoms. The coordination structures of the Rh-Si₄ tetrahedron and the Rh-Si₆ octahedron, along with the Rh-Si bond lengths, are shown on the right in Fig. 1 (b). The octahedron involves significant local distortion, which should induce an asymmetric crystal field around the Rh2 atoms, presumably giving rise to ASOC in BaRhSi₂.

The crystal structure of BaRhSi₂ was directly observed using STEM. Figures 2 (a-d) are annular dark-field (ADF) images taken along the [001], [010], [011], and [101] directions, respectively. The crystal structure model viewed along the corresponding direction is also shown in Fig. 2. The atomic arrangement patterns of the structure model are consistent with the observed STEM-ADF lattice images. Rh and Ba atoms are clearly observable as bright spots in all the images, while Si atoms are dark and inconspicuous in the images. In fact, in Figs. 2 (a) and 2 (b), Si atoms are invisible because they are situated beside prominent spots of Ba and Rh atoms. Nevertheless, in Figs. 2 (c) and 2 (d), Si atoms are obscure spots but faintly observable. In Fig. 2 (c), dim spots (Si) are situated at one of the inline three atoms (Ba-Rh-Si) along the *a*-axis in the hexagonal pattern. Also, in Fig. 2 (d), obscure spots (Si) are detectable inside the triangles of the bright Rh atoms. In these images (Figs. 2 (c) and 2 (d)), the Si atoms are superimposed on each other as a line along the projection direction, enhancing their spot intensity. On the other hand, it was also observed that in Fig. 2 (c) the atomic arrangement is vertically asymmetric, suggesting that there is no mirror plane perpendicular to the *a*-axis in the crystal symmetry; this validates the noncentrosymmetric structure of BaRhSi₂.

B. Superconducting properties

Figure 3 (a) shows the temperature (*T*) dependence of electrical resistivity (ρ) under the magnetic fields $H = 0$ and 55 kOe. A superconducting transition occurs at the critical temperature $T_c \sim 5$ K at zero field, while the superconductivity disappears under $H = 55$ kOe. In the normal state ($T > T_c$), *T*-dependence of the resistivity exhibits metallic behavior like a Bloch-Grüneisen type. No magnetoresistance was observed. The large residual resistivity ($\rho_0 \sim 0.35$ mΩcm) and rather low relative resistance ratio ($\rho_{300K}/\rho_0 \sim 5.8$) suggest that impurities, lattice imperfections, and/or grain boundary scattering dominate electron conduction at low temperatures. This implies a short mean free path *l*. Figure 3 (b) is the *T*-dependence of the electrical resistivity below 8 K under various magnetic

fields. When $H = 0$, the onset T_c ($= T_c^{\text{onset}}$) is ~ 5.5 K, and the zero-resistivity T_c ($= T_c^0$) is ~ 4.7 K. Application of the magnetic fields gradually suppresses the superconductivity. At $H = 35$ kOe, the superconducting transition is almost invisible at 1.9 K.

Figure 4 (a) shows the T -dependence of magnetic susceptibility χ ($\sim M/H$). The diamagnetic signals due to the superconducting transition appear below ~ 5.2 K (onset T_c). The bulk T_c is ~ 5.0 K. The magnetic susceptibility value for the shielding effect at 1.8 K is -1.46×10^{-2} emu/g ($= -8.85 \times 10^{-2}$ emu/cm³), which is almost equal to the full-volume Meissner signal $-1/4\pi$. The large signal ensures that the observed superconductivity is a bulk phenomenon originating from BaRhSi₂. Figure 4 (b) is the M - H hysteresis curve for the superconducting state at 1.8 K. The behavior of the M - H curve is typical of a type-II superconductor.

Specific heat (C_p) data for BaRhSi₂ are plotted as C_p/T versus T^2 in Fig. 5 (a). When $H = 0$, a superconducting transition with a specific-heat jump was observed around $T_c^{\text{onset}} \sim 5.4$ K ($T^2 \sim 29.5$ K²). T_c gradually decreases with increasing H , and the superconductivity is completely suppressed at 50 kOe. At a low-temperature limit, the specific heat for the normal state can be expressed by summation of the electronic term and lattice term as follows:

$$C_p \sim C_v = \gamma_n T + \frac{12\pi^4}{5} r N_A k_B \left(\frac{T}{\Theta_D} \right)^3, \quad (1)$$

where γ_n , Θ_D , N_A , k_B , and r denote Sommerfeld constant, Debye temperature, Avogadro's number, Boltzmann constant, and the number of atoms per molecule, respectively. From the linear extrapolation of the least-squares fit of the $H = 50$ kOe dataset at low temperatures ($T < 3$ K), the Sommerfeld constant $\gamma_n \sim 5.2$ mJ/mole-K² and Debye temperature $\Theta_D \sim 308$ K were determined.

Figure 5 (b) shows the C_{el}/T vs T plots under various magnetic fields. The low-temperature curve (solid line) below 1.9 K was expected by tentatively assuming a BCS-type superconductor [28]. The curve satisfies the requirement that the entropy of the normal state and the superconducting state are equal at T_c ; *i.e.*, $\gamma_n T_c = \int_0^{T_c} \frac{C_{el}}{T} dT$. By idealizing the specific-heat jump to ensure entropy balance around the transition, the bulk thermodynamic critical temperature was determined as $T_c^{\text{bulk}} = 5.1$ K at $H = 0$. For the $H = 0$ curve, the magnitude of the normalized ideal specific-heat jump at T_c^{bulk} is $\Delta C_{el}/\gamma_n T_c \sim 1.43$. This value agrees with the value of 1.43 for a BCS prediction, suggesting that BaRhSi₂ is in the category of weak-coupling superconductors.

For conventional BCS-type superconductors, the strength of the Cooper pairing can be evaluated with the electron-phonon coupling constant λ_{ep} . In this study, λ_{ep} was estimated using the McMillan's formula [29]:

$$T_c = \left(\frac{\Theta_D}{1.45} \right) \exp \left[- \frac{1.04(1+\lambda_{ep})}{\lambda_{ep} - \mu^* (1+0.62\lambda_{ep})} \right], \quad (2)$$

where μ^* is a Coulomb pseudopotential parameter and 0.13 is often used as a standard value [30]. Using the experimental values Θ_D ($= 308$ K) and T_c ($= 5.1$ K), we estimated the moderate value $\lambda_{ep} \sim$

0.6. In solids, effective mass of electrons, *i.e.*, Sommerfeld constant γ_n , is enhanced not only by electron-phonon interaction but also by electronic correlation. The electron-electron coupling constant λ_{ee} has been estimated using the following formula:

$$\gamma_n = \frac{1}{3}\pi^2 k_B^2 N(E_F)(1 + \lambda_{ep})(1 + \lambda_{ee}), \quad (3)$$

where $N(E_F)$ is the DOS of the electronic bands. For BaRhSi₂, $N(E_F)$ was estimated to be ~ 7.5 states/eV/f.u. using the *ab initio* DFT calculation. (See the section, III C.) Substituting this value (7.5 states/eV/f.u.) for $N(E_F)$ into Eq. 3, $\lambda_{ee} \sim 0.1$ was determined. The small λ_{ee} value suggests a conventional Fermi liquid behavior with weak electron correlation. Therefore, phonon mediation seems to dominate Cooper pairing in BaRhSi₂.

Figure 5 (c) shows the C_{el} vs T plots under various magnetic fields. In general, in a superconducting state, heat is carried by thermally excited quasi-particles. Low-temperature electronic specific heat, therefore, reflects its gap structure. For example, the uniform gap (isotropic gap) structure leads to a thermal activation type temperature dependence on the specific heat (*i.e.*, $C_{el} \propto \exp(-\Delta/k_B T)$), whereas for a line-nodal gap (anisotropic gap) state, the specific heat is predicted to be proportional to T -square (*i.e.*, $C_{el} \propto T^2$) at low temperatures [31]. Figure 5 (d) (main panel) shows $C_{el}(T)$ at $H = 0$ in the superconducting state ($T < T_c$), where C_{el} and T are normalized by $\gamma_n T_c$ and T_c , respectively. The solid curve represents the theoretical T -dependence of C_{el} for ideal BCS uniform-gap superconductors by Mühlshlegel [28]. The $C_{el}(T)$ data points (red open circles) are generally consistent with the theoretical curve. The inset shows a semi-logarithmic plot of the reduced electronic specific heat $C_{el}/\gamma_n T_c$ versus inverse reduced temperature T_c/T . This behavior suggests that the activation energy type thermal excitation is dominant at least within the mid temperature range of $0.37 < T/T_c < 0.8$ for the superconducting state in BaRhSi₂. However, the temperature range of this measurement is insufficient to conclusively confirm the fully gapped behavior in this superconducting system. For more detailed discussion of the gap structure and the Cooper pairing state, lower temperature measurements below $T_c/3$ are required.

Figure 6 shows the relationship between the upper critical field H_{c2} and the critical temperature T_c . In this plot, the data points of $T_c(H)$ were obtained from the plots of T -dependent electrical resistivity ρ in Fig. 3 (b) and electronic specific heat C_{el} in Fig. 5 (b) under different magnetic fields. The value of H_{c2} is slightly different depending on the definition of T_c (T_c^{onset} or T_c^{bulk}) and the measured physical properties (ρ or C_{el}). In any datasets, H_{c2} increases rapidly with decreasing temperature. From a rough visual extrapolation of the data plots towards lower temperatures, H_{c2} appears to approach around 30 \sim 40 kOe at $T = 0$ K. In general, for type-II superconductors, the upper critical field $H_{c2}(0)$ depends on both the Pauli limit H_P and the orbital limit H_{orb} . The Pauli limit H_P is due to paramagnetic pair breaking, and corresponds to the magnetic field at which Zeeman splitting energy balances the superconducting condensation energy Δ_0 . Accordingly, H_P can be given by

$$H_P = \frac{\sqrt{2}\Delta_0}{g\mu_B\sqrt{1-\frac{\chi_s}{\chi_n}}}, \quad (4)$$

where g is g -value ($= 2.0$ for free electrons), μ_B is Bohr magneton, and χ_s and χ_n are spin susceptibilities of the superconducting state and Pauli spin susceptibility at T_c in the normal states, respectively [32]. For BaRhSi₂, assuming spin-singlet Cooper pairs ($\chi_s(0) = 0$) and the BCS gap parameter $\Delta_0/k_B T_c \sim 1.764$, the Pauli limit is tentatively estimated as $H_P = 1.857 \times 10^4 T_c \sim 95$ kOe. If the Cooper pairs include spin-triplet component (*i.e.*, $\chi_s(0) \neq 0$), H_P should be greater than 95 kOe. In either case, the expected value of $H_{c2}(0)$ derived from the measured data is clearly less than 95 kOe. This suggests that the actual upper critical field is limited by orbital pair breaking; *i.e.*, $H_{c2}(0) = H_{\text{orb}}$. The Maki parameter α_M is therefore roughly estimated as $\alpha_M = \sqrt{2} H_{\text{orb}}/H_P \sim 0.5$ [33, 34].

Orbital limit H_{orb} is pair breaking due to Lorentz force. H_{orb} is derived from the Ginzburg-Landau (GL) theory as

$$H_{\text{orb}} = \frac{\Phi_0}{2\pi\xi^2}, \quad (5)$$

where Φ_0 is fluxoid quantum and ξ is superconducting coherence length. According to the Werthamer-Helfand-Hohenberg (WHH) theory for conventional weak-coupling BCS-type superconductors, the T -dependent $H_{c2}(T)$ draws a gradual saturation curvature with decreasing T , and crosses the $T = 0$ K axis at a finite orbital limit $H_{\text{orb}}^{\text{BCS}}$, described as $H_{\text{orb}}^{\text{BCS}} = 0.69 \times \left[-\left(\frac{dH_{c2}(T)}{dT} \right) \Big|_{H=0} \right] \times T_c$ for a dirty limit case ($l \ll \xi$) [35, 36]. For BaRhSi₂, the WHH curve expected from the initial gradient of H_{c2} at $H = 0$ is shown as a dotted line in Fig. 6. However, it clearly does not fit the measured data points. Rather, its temperature dependence of the observed H_{c2} appears to consistently curve upwards from T_c to temperatures around $T_c/2$. Such an enhancement of H_{c2} seems to be unexplainable by the moderate electron-phonon coupling ($\lambda_{\text{ep}} \sim 0.6$) in BaRhSi₂ [37]. A similar behavior of the $H_{c2}(T)$ curve has also been reported for some noncentrosymmetric compounds, such as CaIrSi₃ [38]. Several theoretical models have been proposed to explain the enhancement of H_{c2} with positive curvature, including the multi-gap state [39], Fermi surface anisotropy [40], pair-breaking scattering [41], and a local-pairing mechanism [42]. We analyzed the data using the following formula, which allows for an initial upward curvature of $H_{c2}(T)$ in the vicinity below T_c [43]:

$$H_{c2}(T) = H_{c2}(0) \left[1 - \left(\frac{T}{T_c} \right)^{\frac{3}{2}} \right]^{\frac{3}{2}}, \quad (6)$$

where T_c is the transition temperature at zero magnetic field. In Fig. 6, the solid lines show the numerical fittings to the data measured on BaRhSi₂. The fittings yield $H_{c2}(0) \sim 32$ kOe for the bulk value and ~ 42 kOe for the onset of the transition.

Superconducting parameters of BaRhSi₂ were estimated from the specific-heat data, assuming $H_{c2}(0) = 32 \pm 10$ kOe. The error bar (± 10 kOe) originates from the approximate width of the transition,

and it propagates into errors in the calculated superconducting parameters. The thermodynamic critical field $H_c(0)$ can be calculated from the free-energy difference between the superconducting and the normal states, given by the expression $\frac{1}{8\pi}H_c^2(0) = F_n - F_s = -\frac{1}{2}\gamma_n T_c^2 + \int_0^{T_c} C_{el}(T) dT$. The resultant $H_c(0)$ is ~ 407 Oe. The normalized parameter $\gamma_n T_c^2 / H_c^2(0)$ is ~ 0.168 . Lower critical field $H_{c1}(0) \sim 5 \pm 1$ Oe is obtained using the equation $H_c^2 = H_{c1} \times H_{c2}$. The superconducting coherence length and penetration depth were estimated to be $\xi \sim 10 \pm 1$ nm and $\lambda_L \sim 560 \pm 80$ nm using the formulae $H_{c2} = \Phi_0 / 2\pi\xi^2$ and $H_{c1} = \Phi_0 / 4\pi\lambda_L^2$, respectively. The Ginzburg-Landau parameter is $\kappa_{GL} = \lambda_L / \xi \sim 56 \pm 17$, indicating that BaRhSi₂ is a typical type-II superconductor. These parameters are summarized in Table 2 together with other physical properties determined in this work. The superconducting properties of BaRhSi₂ are similar to those of the isostructural compound BaIrSi₂. The T_c of BaIrSi₂ is about 1 K higher than that of BaRhSi₂, despite its smaller DOS at E_F . This is probably due to the stronger electron-phonon interaction in BaIrSi₂ than in BaRhSi₂.

C. DFT Electronic structure

Figure 7 shows the electronic band structure of BaRhSi₂ for scalar-relativistic calculations without SOC (Fig. 7 (a)) and relativistic calculations with SOC (Fig. 7 (b)). There is a small band gap ($\Delta_G \sim 0.12$ eV) at the Γ point just above E_F . Energy bands cross E_F , forming a metallic state in BaRhSi₂, which is consistent with the experimental results of the resistivity and specific-heat measurements. Numerous narrow bands derived from Rh-4*d* orbitals are situated in the valence bands ($E > -5.5$ eV). The band structure in BaRhSi₂ is similar to that in BaIrSi₂ [20].

Figure 8 shows the partial and total DOS ($N(E)$) with SOC. The total DOS clearly indicates that there is a small band gap between the valence bands ($-5.5 \text{ eV} \leq E \leq +0.3 \text{ eV}$) and the unoccupied bands ($E \geq +0.42 \text{ eV}$). The Fermi energy (E_F) is located near the top of the valence bands, giving a finite DOS at E_F ; $N(E_F) \sim 7.5$ states/eV/f.u.. The E_F is situated at the local minimum of the DOS, probably stabilizing the compound. The DOS calculation revealed that the valence bands are mainly derived from Rh-4*d* and Si-3*p* bonding orbitals. The Rh-4*d* orbitals show prominent DOS peaks around $-5 \text{ eV} \leq E \leq -2 \text{ eV}$, due to their narrow-band nature. The Si-3*p* orbitals, which have a relatively broad band character, are hybridized with the Rh-4*d* orbitals in the same energy range, forming the valence bands. The valence bands spread over the energy range beyond E_F . As a result, the DOS at E_F consists mainly of the Rh-4*d* and Si-3*p* hybridized orbitals. On the other hand, the unoccupied bands originate mainly from the Rh-4*d* and Ba-5*d* anti-bonding orbitals. The Ba-5*d* orbital is mainly distributed above E_F . Its contribution to $N(E_F)$ is not so large.

Figures 7 (a) and 7 (b) clearly show that SOC lifts the band degeneracy. At general k -points such as the X- Γ -Y, Y₂-Y, and Γ -Z lines, a twofold spin-degenerating band splits into two sub-bands (bands without spin degeneracy) by SOC. In contrast, on the X₂-Z-Y₂ lines at the Brillouin zone boundary, the twofold band degeneracy remains even with SOC due to the crystal symmetry. The lower panels

of Fig. 7 are close-up views of the band structures near E_F . When SOC is not included, there exist two bands crossing E_F . As shown in Fig. 7 (a), the upper band crosses E_F at the points A, B, and C, while the lower band crosses E_F at the point D. On the X_2-Z-Y_2 lines, these two bands are being degenerate by crystal symmetry. They cross E_F at the points E and F. In Fig. 7 (b), SOC lifts the band degeneracy to modify the Fermi surfaces. On the X_2-Z-Y_2 lines, the band splitting due to SOC is $\Delta_{SO} \sim 0.04$ eV near E_F . On the $X-\Gamma-Y$, Y_2-Y , and $\Gamma-Z$ lines, ASOC splits the band into two sub-bands, which cross E_F at adjacent two points, forming double Fermi surfaces. The band splitting due to ASOC is $\Delta_{ASO} \sim 0.03$ eV near E_F . The band splitting energies in BaRhSi₂ are smaller than those ($\Delta_{SO} \sim 0.12$ eV and $\Delta_{ASO} \sim 0.07$ eV) in BaIrSi₂.

Figures 9 (a) and 9 (b) show the Fermi surfaces in BaRhSi₂ without and with SOC, respectively. When SOC is not included (Fig. 9 (a)), there exist three Fermi surfaces. The first (green curved Fermi surface), which originates in the lower band, is situated around the A_1 point. The second (brown curved Fermi surface), which originates in the upper band, is situated around the Z point. These Fermi surfaces combine together at the $k_z = \pm 1/2$ Brillouin zone boundary. The third (small brown Fermi surface), which is also derived from the upper band, is an electron pocket situated around the midpoint on the $\Gamma-Y$ axis. With SOC (Fig. 9 (b)), the Fermi surfaces split into two for each. At general k -points except on the $k_z = \pm 1/2$ zone boundary, spin degeneracy of the Fermi surface has been solved by ASOC. In total, three pairs of Fermi surfaces split by SOC exist in the Brillouin zone. Most of the conduction electrons, except for $k_z = \pm 1/2$, are free of spin degeneracy. Figure 9 (c) depicts k_x-k_y cross sections of the Fermi surfaces, without SOC (black broken lines) and with SOC (green and brown lines), where two calculation results have been superimposed on the sheet. The typical distance between two spin-splitting Fermi surfaces in a k_x-k_y plane is $\Delta q \sim 0.04$ nm⁻¹, which is about a half of ~ 0.08 nm⁻¹ in BaIrSi₂. The difference in the Fermi surface splitting distance between the two isostructural compounds seems to be mainly due to the difference in the atomic numbers of the constituent elements, ⁴⁵Rh and ⁷⁷Ir. The relativistic effect is smaller in BaRhSi₂ than in BaIrSi₂.

IV. CONCLUSIONS

Noncentrosymmetric superconductivity is one of the recent central issues in the field of strongly correlated electron systems in physics. It is important to search for noncentrosymmetric superconductors for understanding the unconventional superconducting state. In this paper, we have reported the crystal structure, superconducting properties, and DFT electronic structure of a barium-rhodium silicide BaRhSi₂.

BaRhSi₂ crystallizes in an orthorhombic lattice with a noncentrosymmetric space group $C222_1$ and the lattice constants, $a = 14.9777(1)$ Å, $b = 8.0517(1)$ Å and $c = 8.0551(1)$ Å, which is isostructural to

BaIrSi₂. The structure contains significantly distorted Rh-Si₆ octahedrons responsible for ASOC that occurs through an asymmetric crystal field around the Rh atom. Electrical resistivity, magnetic moment and specific-heat measurements clearly indicate that BaRhSi₂ is a type-II superconductor, with $T_c \sim 5.1$ K, $H_{c2}(0) \sim 32$ kOe, and $\kappa_{GL} \sim 56$. The Cooper pairing can be characterized with moderate electron-phonon coupling ($\lambda_{ep} \sim 0.6$), and weak electron correlation ($\lambda_{ee} \sim 0.1$). Phonon mediation seems to dominate Cooper pairing.

The *ab initio* DFT calculation revealed that in BaRhSi₂ the electronic state near E_F mainly consists of the Rh-4*d* and Si-3*p* hybridized orbitals and the SOC lifts the band degeneracy. At general *k*-points except for the Brillouin zone boundary a two-fold spin-degenerating band splits into two sub-bands due to ASOC. The band-splitting energy is around $\Delta_{ASO} \sim 0.03$ eV near E_F . There are three pairs of Fermi surfaces split by SOC. The typical distance between two spin-splitting Fermi surfaces in *k*-space is $\Delta q \sim 0.04$ nm⁻¹, which is about a half of ~ 0.08 nm⁻¹ in BaIrSi₂. The difference in the Fermi surface splitting distance between the two isostructural compounds seems to be mainly due to the difference in the atomic numbers of the constituent elements, ⁴⁵Rh and ⁷⁷Ir. The relativistic effect is smaller in BaRhSi₂ than in BaIrSi₂. Despite the Fermi-surface splitting due to ASOC, superconductivity in the noncentrosymmetric system BaRhSi₂ seems to be almost conventional, except for the anomalous enhancement of $H_{c2}(T)$ with an upward curvature below near T_c .

ACKNOWLEDGMENTS

We thank Dr. T. Taniguchi of the National Institute for Materials Science (NIMS) for technical support in the high-pressure synthesis experiments and Mr. M. Nishio of NIMS for EPMA measurements. This work was partly supported by the Japan Society for the Promotion of Science (JSPS) through Grants-in-Aid for Scientific Research (Grant No. 16K06712, 19K03755). The part of calculations in this study were performed on the Numerical Materials Simulator at NIMS.

DATA AVAILABILITY

The data that support the findings of this article are not publicly available. The data are available from the authors upon reasonable request.

-
- [1] J. Kim, M. Daghofer, A. H. Said, T. Gog, J. van den Brink, G. Khaliullin, and B. J. Kim, Excitonic quasiparticles in a spin-orbit Mott insulator, *Nature Commun.* **5**, 4453 (2014), and references therein.
 - [2] *Non-centrosymmetric Superconductors, Introduction and Overview*, Lecture Notes in Physics Vol.

847, edited by E. Bauer and M. Sigrist (Springer-Verlag, Berlin, Heidelberg, 2012). ISBN 978-3-642-24624-1

- [3] L. P. Gor'kov and E. I. Rashba, Superconducting 2D System with Lifted Spin Degeneracy: Mixed Singlet-Triplet State, *Phys. Rev. Lett.* **87**, 037004 (2001).
- [4] P. A. Frigeri, D. F. Agterberg, A. Koga, and M. Sigrist, Superconductivity without Inversion Symmetry: MnSi versus CePt₃Si, *Phys. Rev. Lett.* **92**, 097001 (2004).
- [5] S. Fujimoto, Electron Correlation and Pairing States in Superconductors without Inversion Symmetry, *J. Phys. Soc. Jpn.* **76**, 051008 (2007).
- [6] S. Fujimoto, Fermi Liquid Theory for Heavy Fermion Superconductors without Inversion Symmetry: Magnetism and Transport Coefficients, *J. Phys. Soc. Jpn.* **76**, 034712 (2007).
- [7] S. Fujimoto, Emergent Nodal Excitations due to Coexistence of Superconductivity and Antiferromagnetism: Cases with and without Inversion Symmetry, *J. Phys. Soc. Jpn.* **75**, 083704 (2006).
- [8] S. Fujimoto, Magnetoelectric effects in heavy-fermion superconductors without inversion symmetry, *Phys. Rev. B* **72**, 024515 (2005).
- [9] N. Hayashi, K. Wakabayashi, P. A. Frigeri, and M. Sigrist, Temperature dependence of the superfluid density in a noncentrosymmetric superconductor, *Phys. Rev. B* **73**, 024504 (2006)
- [10] N. Hayashi, K. Wakabayashi, P. A. Frigeri, and M. Sigrist, Nuclear magnetic relaxation rate in a noncentrosymmetric superconductor, *Phys. Rev. B* **73**, 092508 (2006).
- [11] M. Nishiyama, Y. Inada, and Guo-qing Zheng, Spin Triplet Superconducting State due to Broken Inversion Symmetry in Li₂Pt₃B, *Phys. Rev. Lett.* **98**, 047002 (2007).
- [12] H. Q. Yuan, D. F. Agterberg, N. Hayashi, P. Badica, D. Vandervelde, K. Togano, M. Sigrist, and M. B. Salamon, S-Wave Spin-Triplet Order in Superconductors without Inversion Symmetry: Li₂Pd₃B and Li₂Pt₃B, *Phys. Rev. Lett.* **97**, 017006 (2006).
- [13] S. Harada, J. J. Zhou, Y. G. Yao, Y. Inada, and G.-Q. Zheng, Abrupt enhancement of noncentrosymmetry and appearance of a spin-triplet superconducting state in Li₂(Pd_{1-x}Pt_x)₃B beyond $x = 0.8$, *Phys. Rev. B* **86**, 220502(R) (2012).
- [14] E. Bauer, G. Hilscher, H. Michor, Ch. Paul, E. W. Scheidt, A. Griбанov, Yu. Seropegin, H. Noël, M. Sigrist, and P. Rogl, Heavy Fermion Superconductivity and Magnetic Order in Noncentrosymmetric CePt₃Si, *Phys. Rev. Lett.* **92**, 027003 (2004).
- [15] N. Kimura, K. Ito, K. Saitoh, Y. Umeda, H. Aoki, and T. Terashima, Pressure-Induced Superconductivity in Noncentrosymmetric Heavy-Fermion CeRhSi₃, *Phys. Rev. Lett.* **95**, 247004 (2005).
- [16] I. Sugitani, Y. Okuda, H. Shishido, T. Yamada, A. Thamizhavel, E. Yamamoto, T.D. Matsuda, Y. Haga, T. Takeuchi, R. Settai, and Y. Ōnuki, Pressure-Induced Heavy-Fermion Superconductivity in Antiferromagnet CeIrSi₃ without Inversion Symmetry, *J. Phys. Soc. Jpn.* **75**, 043703 (2006).

- [17] A. D. Hillier, J. Quintanilla, and R. Cywinski, Evidence for Time-Reversal Symmetry Breaking in the Noncentrosymmetric Superconductor LaNiC_2 , *Phys. Rev. Lett.* **102**, 117007 (2009).
- [18] R. P. Singh, A. D. Hillier, B. Mazidian, J. Quintanilla, J. F. Annett, D. McK. Paul, G. Balakrishnan, and M. R. Lees, Detection of Time-Reversal Symmetry Breaking in the Noncentrosymmetric Superconductor Re_6Zr Using Muon-Spin Spectroscopy, *Phys. Rev. Lett.* **112**, 107002 (2014).
- [19] T. Shang, S. K. Ghosh, J. Z. Zhao, L.-J. Chang, C. Baines, M. K. Lee, D. J. Gawryluk, M. Shi, M. Medarde, J. Quintanilla, and T. Shiroka, Time-reversal symmetry breaking in the noncentrosymmetric Zr_3Ir superconductor, *Phys. Rev. B* **102**, 020503(R) (2020).
- [20] M. Isobe, K. Kimoto, M. Arai, and E. Takayama-Muromachi, Superconductivity in BaIrSi_2 : A $5d$ electron system with a noncentrosymmetric crystal structure, *Phys. Rev. B* **99**, 054514 (2019).
- [21] K. Kimoto, T. Asaka, X. Yu, T. Nagai, Y. Matsui, and K. Ishizuka, Local crystal structure analysis with several picometer precision using scanning transmission electron microscopy, *Ultramicroscopy* **110**, 778 (2010).
- [22] F. Izumi and K. Momma, Three-Dimensional Visualization in Powder Diffraction, *Solid State Phenom.* **130**, 15 (2007).
- [23] P. Blaha, K. Schwarz, G. K. H. Madsen, D. Kvasnicka, J. Luitz, R. Laskowski, F. Tran, and L. D. Marks, *WIEN2k: An Augmented Plane Wave Plus Local Orbitals Program for Calculating Crystal Properties* (Karlheinz Schwarz, Techn. Universität Wien, Wien, Austria, 2001). ISBN 3-9501031-1-2. <https://euler.phys.cmu.edu/cluster/WIEN2k/usersguide.html>
- [24] P. Blaha, K. Schwarz, F. Tran, R. Laskowski, G. K. H. Madsen and L. D. Marks, WIEN2k: An APW+lo program for calculating the properties of solids, *J. Chem. Phys.* **152**, 074101 (2020).
- [25] J. P. Perdew, K. Burke, and M. Ernzerhof, Generalized Gradient Approximation Made Simple, *Phys. Rev. Lett.* **77**, 3865 (1996).
- [26] P. Hohenberg and W. Kohn, Inhomogeneous Electron Gas, *Phys. Rev.* **136**, B864 (1964).
- [27] Strictly, small quantities of the impurity phases, RhSi , Ba_2SiO_4 , and BaRhSi_3 , were detected in the BaRhSi_2 sample. RhSi (Fersilicite- FeSi type; $P2_13$; $a \sim 4.69 \text{ \AA}$) is a superconductor with $T_c \sim 0.35 \text{ K}$. Ba_2SiO_4 (β - K_2SO_4 type; $Pnma$; $a \sim 7.51 \text{ \AA}$, $b \sim 5.81 \text{ \AA}$, and $c \sim 10.21 \text{ \AA}$) is an insulating phase. BaRhSi_3 (BaNiSn_3 type; $I4mm$; $a \sim 4.37 \text{ \AA}$ and $c \sim 10.12 \text{ \AA}$) is a superconductor with $T_c \sim 1.3 \text{ K}$, recently discovered by the present authors. Details will be published elsewhere.
- [28] B. Mühlischlegel, Die thermodynamischen Funktionen des Supraleiters, *Z. Phys.* **155**, 313 (1959).
- [29] W. L. McMillan, Transition Temperature of Strong-Coupled Superconductors, *Phys. Rev.* **167**, 331 (1968).
- [30] P. Morel and P. W. Anderson, Calculation of the Superconducting State Parameters with Retarded Electron-Phonon Interaction, *Phys. Rev.* **125**, 1263 (1962).
- [31] G. E. Volovik and L. P. Gor'kov, Superconducting classes in heavy-fermion systems, *Sov. Phys. JETP* **61**, 843 (1985).

- [32] A. M. Clogston, Upper Limit for the Critical Field in Hard Superconductors, *Phys. Rev. Lett.* **9**, 266 (1962).
- [33] K. Maki and T. Tsuneto, Pauli Paramagnetism and Superconducting State, *Prog. Theor. Phys.* **31**, 945 (1964).
- [34] R. R. Hake, UPPER-CRITICAL-FIELD LIMITS FOR BULK TYPE-II SUPERCONDUCTORS, *Appl. Phys. Lett.* **10**, 189 (1967).
- [35] E. Helfand and N. R. Werthamer, Temperature and Purity Dependence of the Superconducting Critical Field, H_{c2} . II, *Phys. Rev.* **147**, 288 (1966).
- [36] N. R. Werthamer, E. Helfand, and P. C. Hohenberg, Temperature and Purity Dependence of the Superconducting Critical Field, H_{c2} . III. Electron Spin and Spin-Orbit Effects, *Phys. Rev.* **147**, 295 (1966).
- [37] L. N. Bulaevskii, O. V. Dolgov, and M. O. Ptitsyn, Properties of strong-coupled superconductors, *Phys. Rev. B* **38**, 11290 (1988).
- [38] G. Eguchi, D. C. Peets, M. Kriener, Y. Maeno, E. Nishibori, Y. Kumazawa, K. Banno, S. Maki, and H. Sawa, Crystallographic and superconducting properties of the fully gapped noncentrosymmetric $5d$ -electron superconductors CaMSi_3 ($M = \text{Ir, Pt}$), *Phys. Rev. B* **83**, 024512 (2011).
- [39] I. N. Askerzade, A. Gencer, and N. Güçlü, On the Ginzburg-Landau analysis of the upper critical field H_{c2} in MgB_2 , *Supercond. Sci. Technol.* **15**, L13 (2002).
- [40] P. C. Hohenberg and N. R. Werthamer, Anisotropy and Temperature Dependence of the Upper Critical Field of Type-II Superconductors, *Phys. Rev.* **153**, 493 (1967).
- [41] V. G. Kogan and R. Prozorov, Orbital upper critical field of type-II superconductors with pair breaking, *Phys. Rev. B* **88**, 024503 (2013).
- [42] R. Micnas, J. Ranninger, and S. Robaszkiewicz, Superconductivity in narrow-band systems with local nonretarded attractive interactions, *Rev. Mod. Phys.* **62**, 113 (1990).
- [43] M. D. Lan, J. C. Chang, K. T. Lu, C. Y. Lee, H. Y. Shih, and G. Y. Jeng, Upper critical field of borocarbide superconductors, *IEEE Trans. Appl. Supercond.* **11**, 3607 (2001).

Table 1. Atomic coordinates (x, y, z), isotropic displacement parameters B , and crystallographic data of BaRhSi₂.

Atom	Site	$g^{\text{a)}$	x	y	z	B (Å ²)
Ba1	4 <i>b</i>	1	0	0.2433(3)	1/4	0.54(4)
Rh1	4 <i>b</i>	1	0	0.2385(4)	3/4	0.63(5)
Ba2	4 <i>a</i>	1	0.1379(1)	0	1/2	1.11(5)
Ba3	4 <i>a</i>	1	0.1321(1)	1/2	0	0.51(5)
Rh2	8 <i>c</i>	1	0.2208(1)	0.3776(4)	0.3747(4)	0.76(3)
Si1	8 <i>c</i>	1	0.2267(3)	0.1580(10)	0.1570(11)	-0.93(11)
Si2	8 <i>c</i>	1	0.1022(4)	0.6053(20)	0.3892(21)	2.37(19)
Si3	8 <i>c</i>	1	0.1157(3)	0.9041(14)	0.1133(16)	0.00(14)
Formula	(asymmetric structure unit)	Ba ₃ Rh ₃ Si ₆				
Molecular weight		889.211				
Space group		<i>C</i> 222 ₁ (No. 20)				
Lattice constants		$a = 14.9777(1)$ Å, $b = 8.0517(1)$ Å, $c = 8.0551(1)$ Å, $V = 971.42(2)$ Å ³				
<i>Z</i>		4				
Density (calcd.)		6.080 g/cm ³				
Temperature		r.t.				
Wavelength		1.540593 Å (Cu K α)				
<i>R</i> -factors		$R_{\text{WP}} = 6.89$ %, $R_{\text{p}} = 5.27$ %, $R_{\text{B}} = 1.29$ %, $R_{\text{F}} = 0.50$ %, $S = R_{\text{WP}}/R_{\text{e}} = 0.949$				
Refinement software		RIETAN-FP				

^a) Occupancies for all the atoms are fixed to 1: $g = 1$.

Table 2. Superconducting parameters for BaRhSi₂. The values for BaIrSi₂ are also given as a matter of comparison.

	BaRhSi ₂ (this work)	BaIrSi ₂ [20]
Onset critical temperature, T_c^{onset}	5.4 K	6.3 K
Bulk critical temperature, T_c^{bulk}	5.1 K	5.8 K
Thermodynamic critical field, $H_c(0)$	407 Oe	490 Oe
Upper critical field, $H_{c2}(0)$	32 ± 10 kOe ^{a)}	60 kOe
Lower critical field, $H_{c1}(0)$	5 ± 1 Oe ^{a)}	4 Oe
Coherence length, ξ	10 ± 1 nm ^{a)}	7.4 nm
Penetration depth, λ_L	560 ± 80 nm ^{a)}	640 nm
Ginzburg-Landau parameter, κ_{GL}	56 ± 17 ^{a)}	87
Specific-heat jump, $\Delta C_{el}(T_c)/\gamma_n T_c$	1.43	1.65
Ratio of critical temperature and field, $\gamma_n T_c^2/H_c^2(0)$	0.168	0.162
Electron-phonon coupling constant, λ_{ep}	0.6	0.8
Electron-electron coupling constant, λ_{ee}	0.1	0.2
Density of states, $N(E_F)$ ^{b)}	7.5 state/eV/f.u.	6.8 state/eV/f.u.
Residual resistivity ρ_0	0.35 mΩcm	0.53 mΩcm
Sommerfeld constant, γ_n	5.2 mJ/mole-K ²	5.5 mJ/mole-K ²
Debye temperature, Θ_D	308 K	305 K

^{a)} The error bars are based on the width of the superconducting transition.

^{b)} estimated by the *ab initio* DFT calculation. Formula unit: Ba₆M₆Si₁₂ ($M = \text{Rh or Ir}$)

FIGURES

FIG. 1. (Color online)

(a) Powder x-ray diffraction (XRD) pattern (x-ray Rietveld analysis profile) of the BaRhSi₂ sample: observed data (red crosses), calculated profile (green solid line), and its differences (blue solid line). The vertical tick marks indicate the Bragg angles for the majority phase BaRhSi₂ (top row) and the small amounts of impurity phases, RhSi (second row), Ba₂SiO₄ (third row), and BaRhSi₃ (bottom row). The refined structural parameters are summarized in Table 1. (b) The crystal structure of BaRhSi₂. The ligands and bond lengths of the Rh1-Si tetrahedron and the Rh2-Si octahedron are shown on the right.

FIG. 2. (Color online)

STEM-ADF images for BaRhSi₂, projected along the (a) [001], (b) [010], (c) [011], and (d) [101] directions. The atomic positions can be identified by comparing them with the crystal structure model viewed along the corresponding direction.

FIG. 3. (Color online)

(a) Temperature (T) dependence of electrical resistivity (ρ) under the magnetic fields $H = 0$ and 55 kOe for a BaRhSi₂ polycrystalline sample. Superconductivity occurs at $T_c \sim 5$ K under $H = 0$. (b) Magnetic-field response of the superconducting transition: $H = 0, 2.5, 5, 7.5, 10, 15, 20, 25, 30, 35, 40, 45, 50$, and 55 kOe. The superconductivity is suppressed around $H \sim 35$ kOe at 1.9 K.

FIG. 4. (Color online)

(a) Temperature dependence of magnetic susceptibility χ ($\sim M/H$) for BaRhSi₂. The data were collected for a powder sample under $H = 10$ Oe in heating process after zero-field cooling (ZFC) and field cooling (FC). (b) Magnetization curve (M - H hysteresis curve) for the superconducting state at 1.8 K. The inset shows magnifications of the low and high magnetic field regions.

FIG. 5. (Color online)

Specific heat for BaRhSi₂, measured under the various magnetic fields $H = 0, 2.5, 5, 7.5, 10, 12.5, 15, 17.5, 20, 22.5, 25$, and 50 kOe. (a) C_p/T vs T^2 plots, where C_p is the measured value, and the solid straight line is a linear extrapolation of the least-squares fit of the data points below 3 K in the normal state at $H = 50$ kOe. The Sommerfeld constant is $\gamma_n \sim 5.2$ mJ/mole-K², while the Debye temperature is $\Theta_D \sim 308$ K. (b) Electronic specific heat C_{el}/T vs T plots, where the solid line below 1.9 K is an expected curvature for a typical BCS-type superconductor [28]. The dashed line near T_c is an extrapolation of the dataset at $H = 0$, giving a bulk thermodynamic critical temperature $T_c^{\text{bulk}} = 5.1$ K, and a normalized specific-heat jump $\Delta C_{el}/\gamma_n T_c \sim 1.43$. The electronic specific heat (C_{el}/T)

complemented by these curves satisfies the condition that the entropy of the superconducting state and the normal state coincide at T_c ; *i.e.*, $\gamma_n T_c = \int_0^{T_c} \frac{C_{el}}{T} dT$. (c) Electronic specific heat C_{el} vs T plots. (d) Dependence of the reduced electronic specific heat $C_{el}/\gamma_n T_c$ on the reduced temperature T/T_c at $H = 0$ in the superconducting state ($T/T_c < 1$), where the solid line represents the theoretical curve for BCS superconductors by Mühlischlegel [28]. The inset shows a semi-logarithmic plot of the reduced electronic specific heat versus inverse of the reduced temperature.

FIG. 6. (Color online)

Upper critical field H_{c2} plotted as a function of T . The data points are provided using the transition temperatures T_c^{onset} , T_c^{mid} and T_c^0 from the electrical resistivity measurements and T_c^{onset} and T_c^{bulk} from the electronic specific heat measurements. The solid curves show the numerical data fit using the formula $H_{c2}(T) = H_{c2}(0)[1 - (T/T_c)^{3/2}]^{3/2}$, which allows for an initial upward curvature of $H_{c2}(T)$ in the vicinity below T_c [43]. The fittings gives $H_{c2}(0) \sim 32$ kOe for the bulk value and ~ 42 kOe for the onset of the transition. The convex dotted line indicates the theoretical $H_{c2}(T)$ curve for dirty-limit BCS weak-coupling superconductors given by Werthamer-Helfand-Hohenberg (WHH) [35, 36]. This curve does not meet the measured data points.

FIG. 7.

Electronic band structure of BaRhSi₂: (a) scalar-relativistic calculations without SOC and (b) relativistic calculations with SOC. The lower panels show close-up views of the band structure near E_F . The codes of the symmetry points (Γ , X, Y, Z, X₂, and Y₂) in the Brillouin zone are shown in Fig. 9. The symbols (A) ~ (F) indicate the intersection points between the bands and the Fermi level E_F .

FIG. 8. (Color online)

Total and partial electronic DOS of BaRhSi₂, for the relativistic calculations with SOC. The values are for a primitive unit cell (*i.e.*, a half of the conventional base-centered orthorhombic unit cell; f.u. = Ba₆Rh₆Si₁₂).

FIG. 9. (Color online)

(a), (b) Fermi surface shapes in BaRhSi₂ for the calculations without and with SOC, respectively. (c) k_x - k_y cross-sections of the Fermi surfaces without SOC (black broken lines) and with SOC (green and brown lines), where two calculation results have been superimposed on the sheet. The blue line indicates the irreducible Brillouin zone (IBZ). The labels indicate symmetry points for the orthorhombic base-centered lattice: $\Gamma = (0,0,0)$, X = (1/2,0,0), Y = (0,1/2,0), Z = (0,0,1/2), X₂ = (1/2,0,1/2), and Y₂ = (0,1/2,1/2).

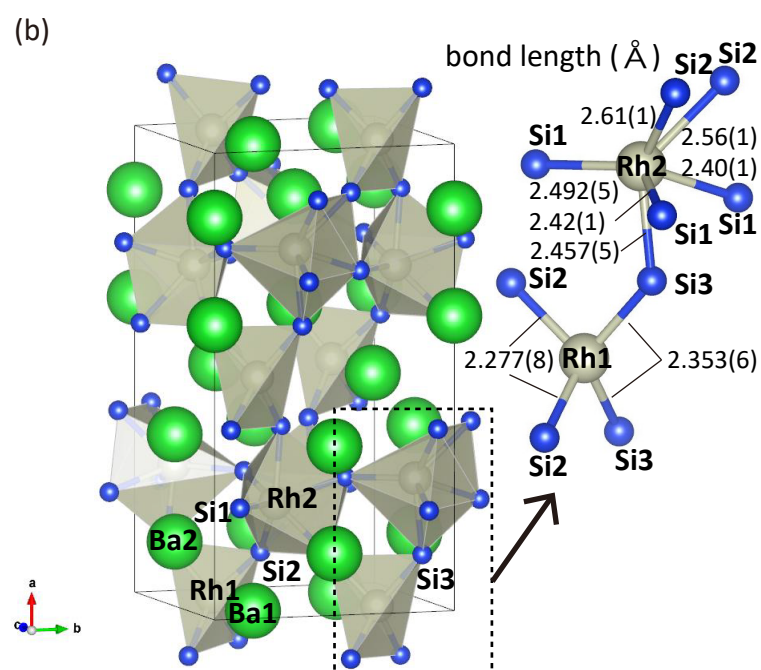
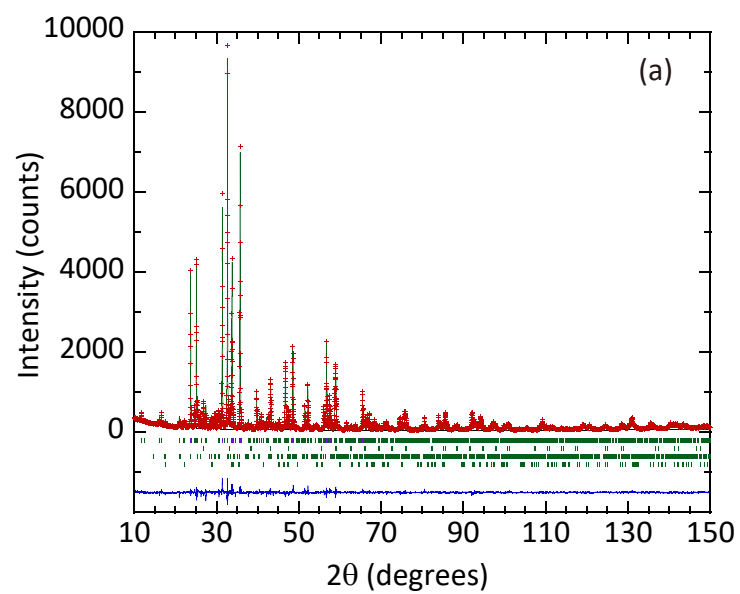


FIG. 1

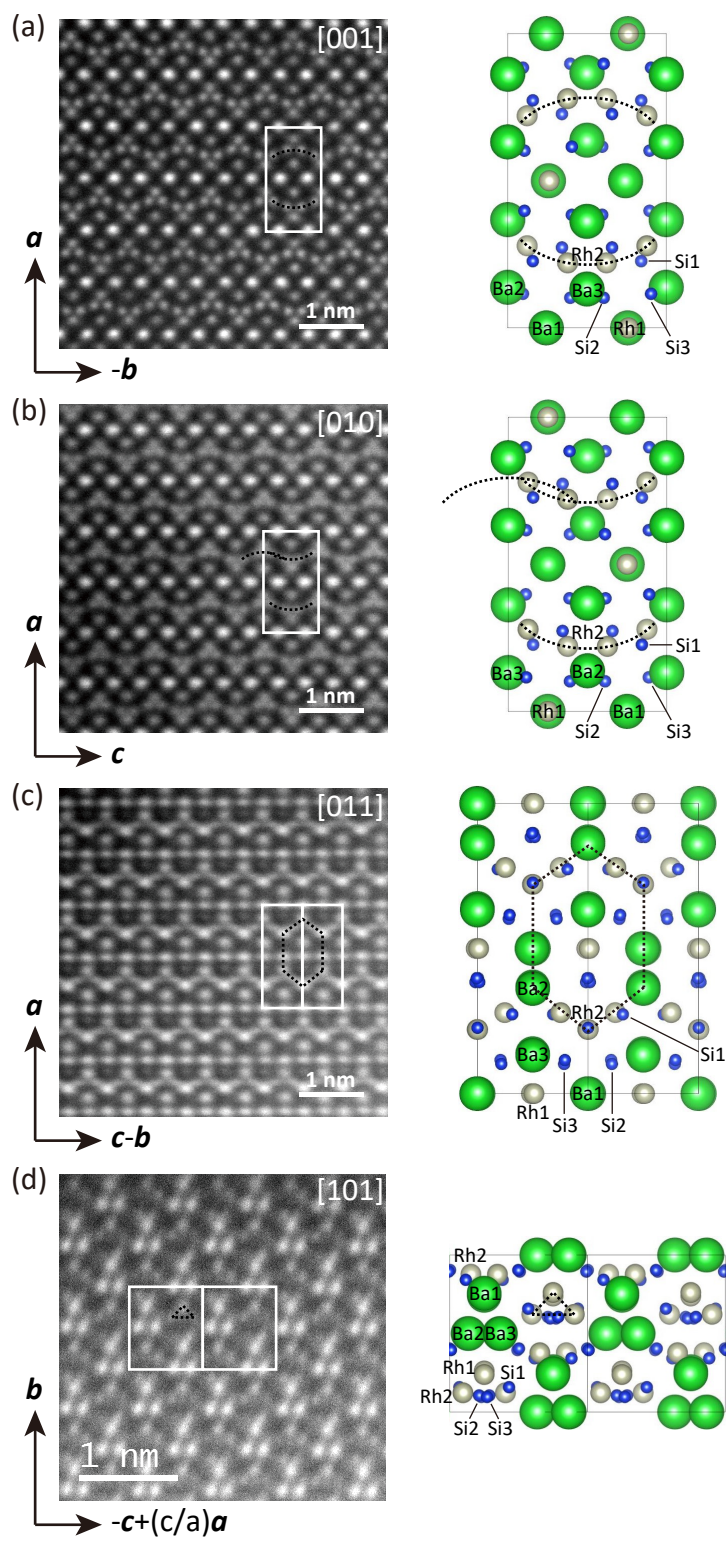


FIG. 2

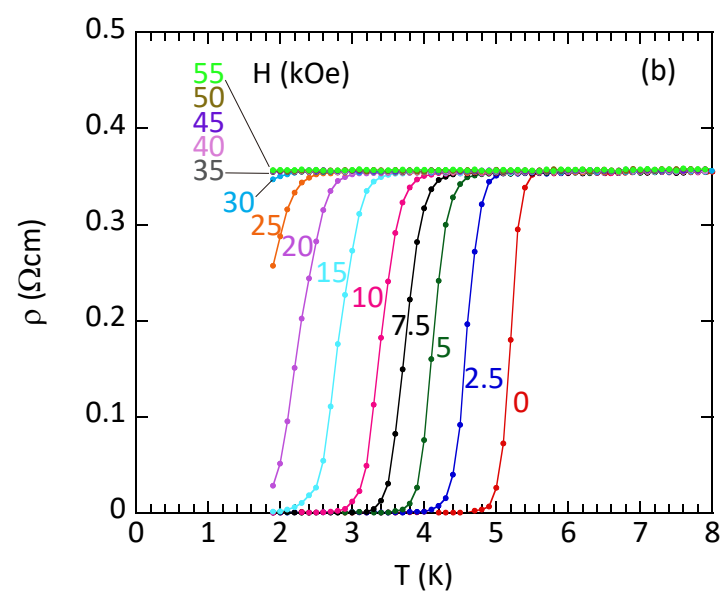
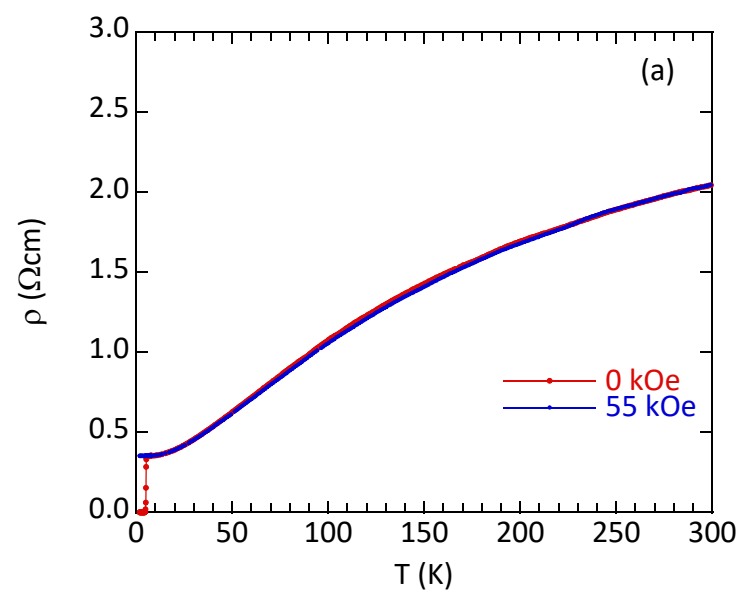


FIG. 3

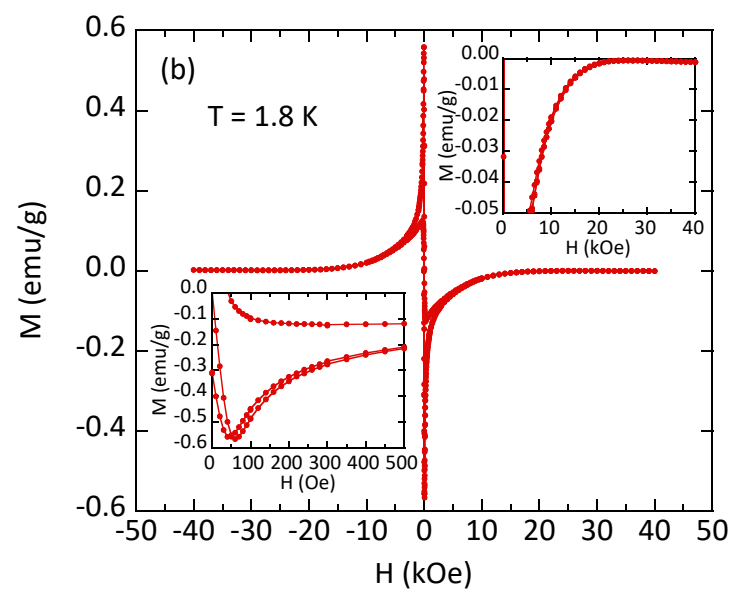
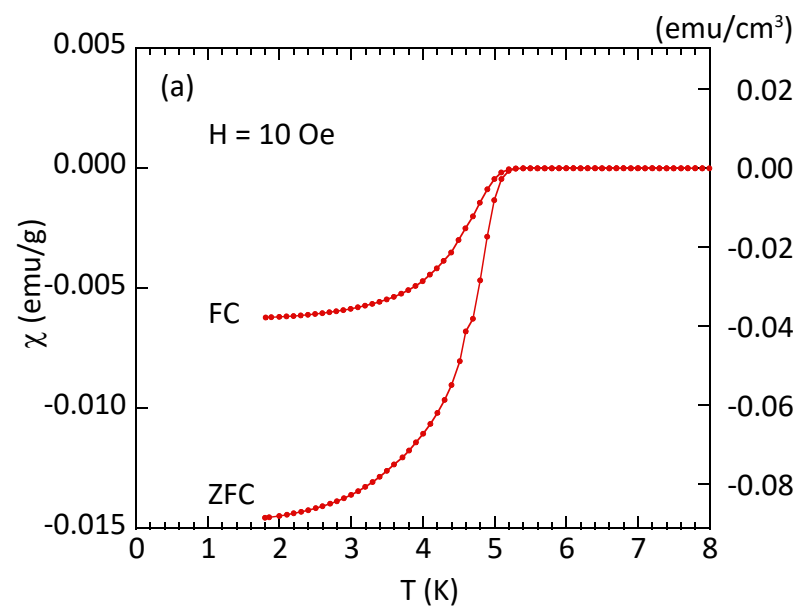


FIG. 4

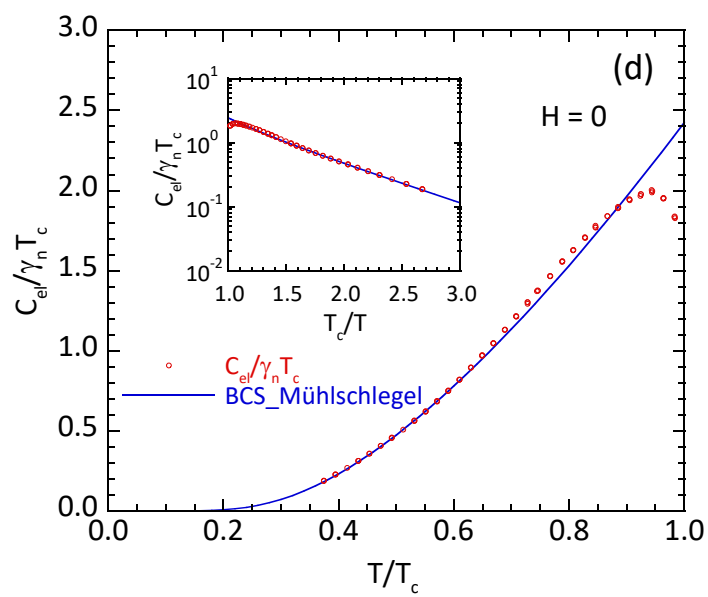
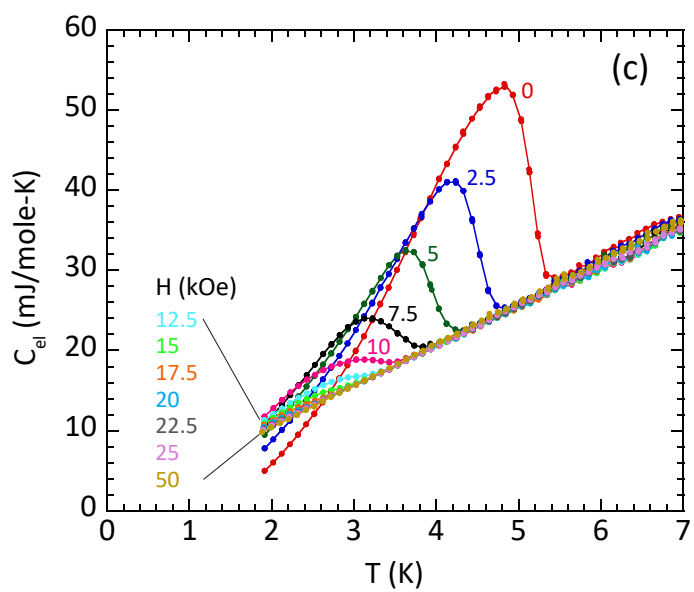
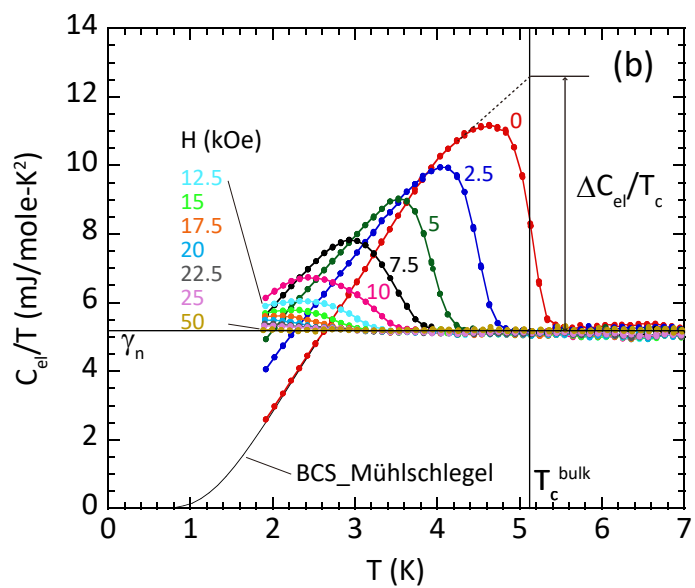
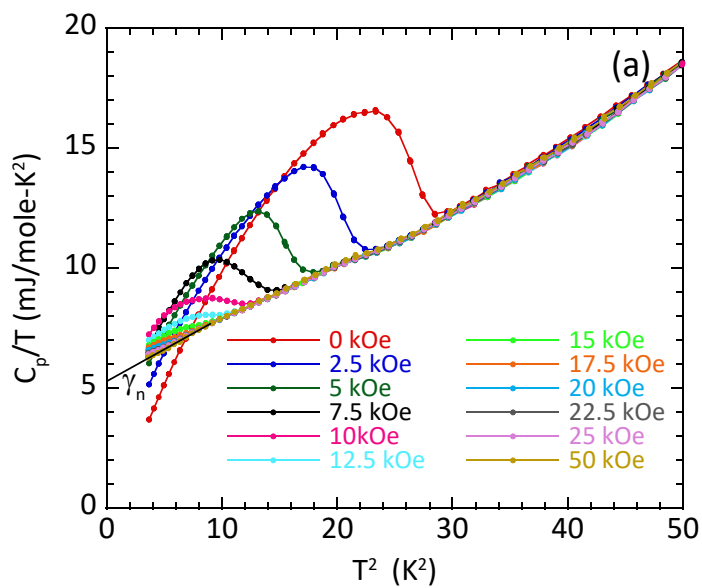


FIG. 5

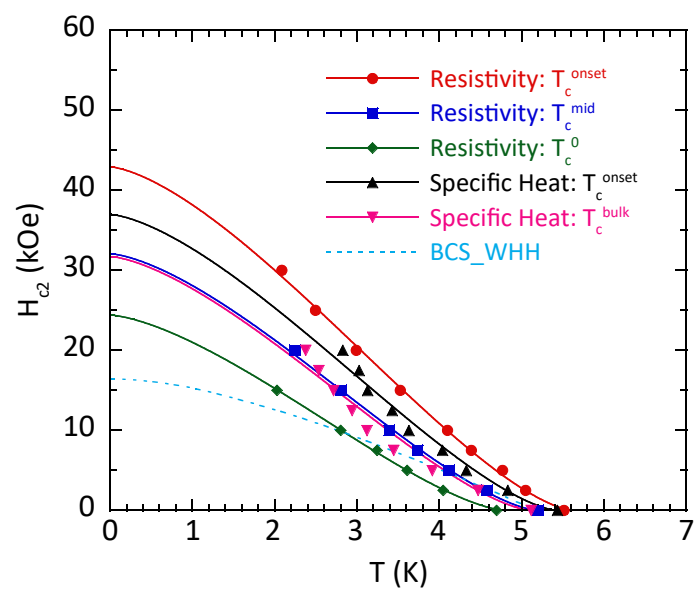


FIG. 6

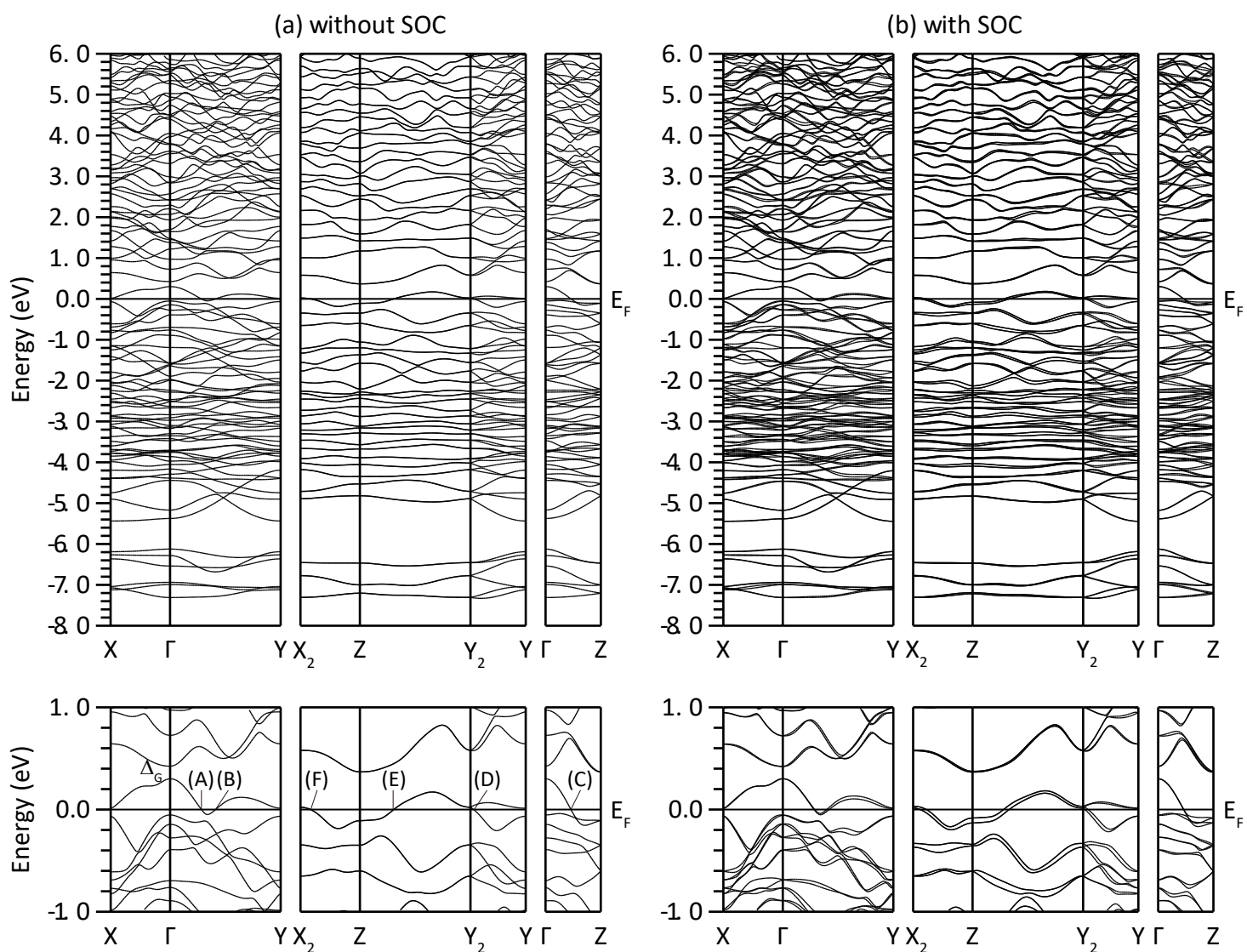


FIG. 7

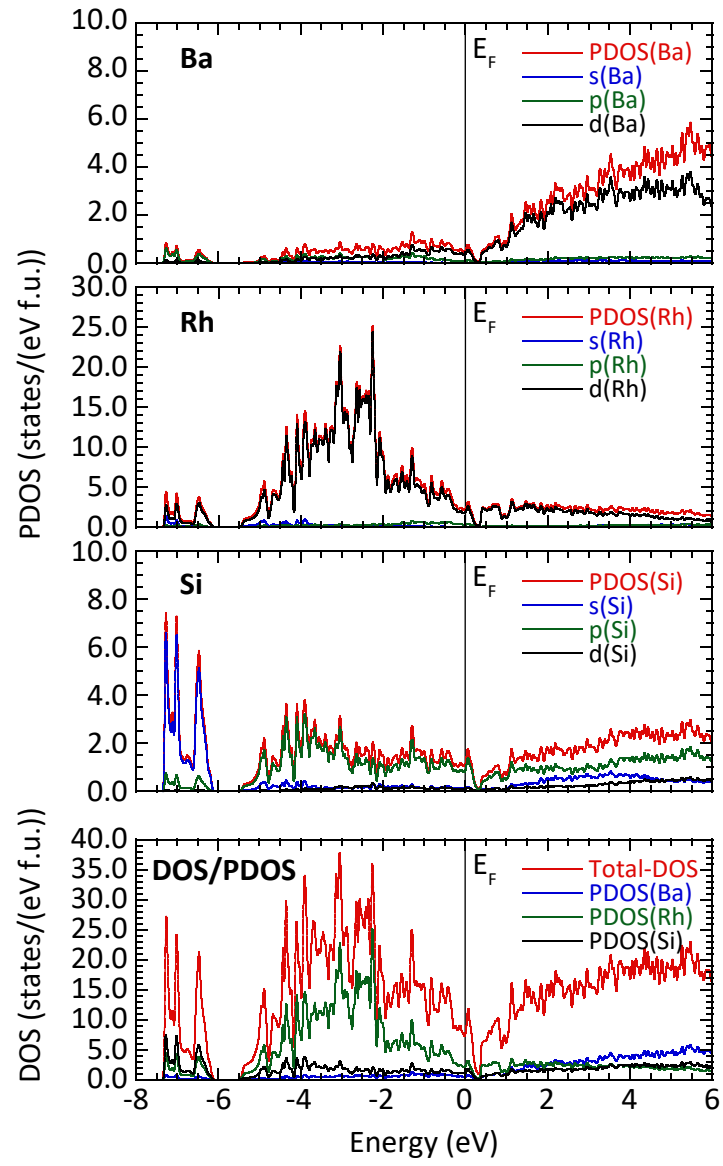
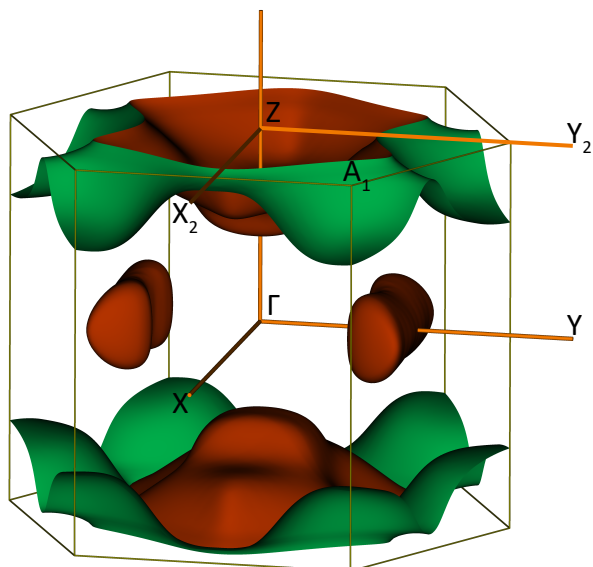
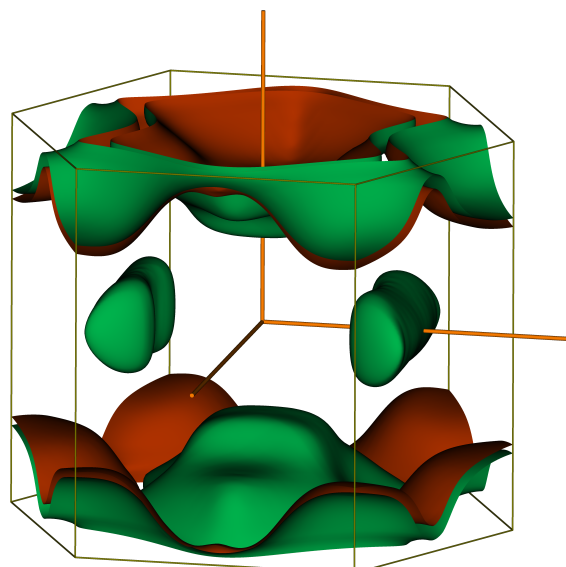


FIG. 8

(a) without SOC



(b) with SOC



(c)

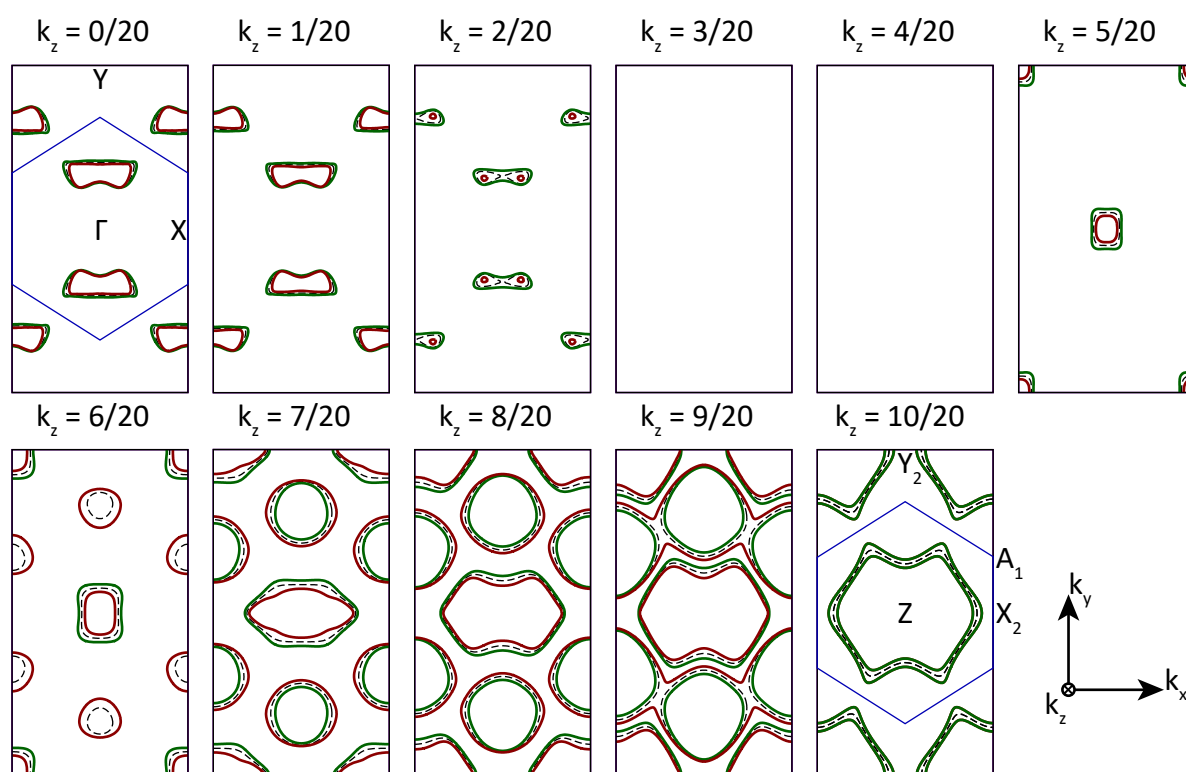


FIG. 9